



Iron isotopic fractionation in mineral phases from Earth's lower mantle: Did terrestrial magma ocean crystallization fractionate iron isotopes?

HPSTAR
684-2019

Hong Yang^{a,1}, Jung-Fu Lin^{b,*}, Michael Y. Hu^c, Mathieu Roskosz^d, Wenli Bi^{c,e}, Jiyong Zhao^c, Esen E. Alp^c, Jin Liu^b, Jiachao Liu^b, Renata M. Wentzowitch^f, Takuo Okuchi^g, Nicolas Dauphas^{h,*}

^a Center for High Pressure Science and Technology Advanced Research (HPSTAR), Pudong, Shanghai 201203, China

^b Department of Geological Sciences, Jackson School of Geosciences, University of Texas at Austin, Austin, TX 78712, USA

^c Advanced Photon Source, Argonne National Laboratory, Argonne, IL 60439, USA

^d IMPMC – UMR CNRS 7590, Sorbonne Universités, UPMC, IRD, MNHN, Muséum National d'Histoire Naturelle, 61 rue Buffon, 75005 Paris, France

^e Department of Geology, University of Illinois at Urbana-Champaign, Urbana, IL 61801, USA

^f Department of Applied Physics and Applied Mathematics and Department of Earth and Environmental Sciences, Lamont-Doherty Earth Observatory, Columbia University, New York, NY 10027, USA

^g Institute for Planetary Materials, Okayama University, Misasa, Tottori 682-0193, Japan

^h Origins Laboratory, Department of the Geophysical Sciences and Enrico Fermi Institute, The University of Chicago, Chicago, IL 60637, USA

ARTICLE INFO

Article history:

Received 11 March 2018

Received in revised form 9 August 2018

Accepted 24 October 2018

Available online xxxx

Editor: B. Buffett

Keywords:

nuclear resonant spectroscopy

iron isotopic fractionation

spin transition

magma ocean crystallization

ABSTRACT

Iron is the most abundant transition metal in the Earth's interior, yet considerable uncertainties remain as to why mantle-derived rocks have diverse iron isotopic compositions. In particular, the isotopic fractionation behavior of iron in the lower-mantle minerals bridgmanite and ferropericlase are largely unexplored. The reason is that it is challenging to study isotopic fractionation at the high pressures relevant to the deep mantle. Here we report *in situ* measurements of the mean force constants of iron bonds in these minerals pressurized in diamond anvil cells using the technique of nuclear resonant inelastic X-ray scattering (NRIXS). We find that the transition from high- to low-spin iron in ferropericlase ((Mg_{0.75}Fe_{0.25})O) at approximately 60 GPa drastically stiffens its iron bonds in the low-spin state. The mean force constant of iron bonds in both Fe-bearing and (Fe,Al)-bearing bridgmanite exhibits softening by 21% at approximately 40–60 GPa, which seems to be associated with changes in the iron local environment during the transition from low to high quadrupole splitting states. These results indicate that in the lower mantle, low-spin ferropericlase is enriched in heavy iron isotopes relative to bridgmanite and metallic iron by +0.15‰ and +0.12‰, respectively. Based on these results, we investigate whether terrestrial magma ocean crystallization could have fractionated iron isotopes. We conclude that this process cannot be responsible for the heavy iron isotope enrichment measured in terrestrial basalts.

© 2018 Elsevier B.V. All rights reserved.

1. Introduction

The +0.1‰ heavy iron isotope enrichment (expressed in $\delta^{56}\text{Fe}$, the deviation in permil of $^{56}\text{Fe}/^{54}\text{Fe}$ ratios relative to reference material IRMM-014) of mid-ocean ridge basalts (MORBs) relative to

chondrites (Teng et al., 2013) distinguishes the Earth from other planetary bodies, such as Mars and Vesta, whose crustal rocks exhibit a similar iron isotopic signature to chondrites (Poitras et al., 2004; Wang et al., 2012). Core formation, as the most significant differentiation event in Earth's history, shaped the chemistry of the mantle, most obviously by scavenging Fe, Ni and siderophile elements into the core. Whether a similar imprint was left in the stable isotopic composition of mantle rocks, in particular for iron, is much more uncertain and is a topic of active research (e.g. Polyakov, 2009; Shahar et al., 2016; Liu et al., 2017; Elardo and Shahar, 2017; Bourdon et al., 2018). The most recent results suggest that due to the comparable strengths of the iron

* Corresponding authors.

E-mail addresses: afu@jsg.utexas.edu (J.-F. Lin), dauphas@uchicago.edu (N. Dauphas).

¹ Now at Department of Geological Sciences, Stanford University, Stanford, CA 94305, USA.

bonds in Fe^{2+} -bearing silicate glasses and metal alloys at high pressure, and the high temperatures involved (~ 3000 – 4000 K), core formation likely played a minor role in fractionating iron isotopes (Liu et al., 2017). Other hypotheses for the superchondritic iron isotopic composition of terrestrial basalts include mantle partial melting (Dauphas et al., 2009) and early evaporation processes (Poitrasson et al., 2004). Magma ocean crystallization could also have fractionated the stable isotopic composition of elements such as silicon (Huang et al., 2014) but iron isotopic fractionation in this process has been largely unexplored.

The most abundant iron-bearing phases in the lower mantle are bridgmanite (Bm) and ferropericlase (Fp). As such, they control how iron isotopes will be fractionated at the interface between the core and mantle or during magma ocean crystallization. Pressure-induced spin transitions of iron in both minerals have been documented to significantly influence their elastic, transport, rheological, and geochemical properties (e.g., Lin et al., 2005, 2013; Wentzcovitch et al., 2009; Wu et al., 2013). The spin transition of Fe^{2+} in Fp with a composition $(\text{Mg}_{0.75}\text{Fe}_{0.25})\text{O}$ occurs at 80–110 GPa along a mantle geotherm (Mao et al., 2011a), which is associated with a $\sim 2\%$ volume decrease and presumably a shortening of the iron bonds by at least 0.7% (Lin et al., 2013). The spin transition is thus expected to influence iron isotopic fractionation significantly. On the other hand, Bm contains both Fe^{2+} and Fe^{3+} ions in the large pseudo-dodecahedral (8/12-fold) A-site as well as Fe^{3+} in the small 6-fold, octahedral B-site (Hsu et al., 2011; Lin et al., 2013). In a pyrolitic lower-mantle composition, most Fe^{3+} will be distributed in the A-site due to the charge-coupled substitution of approximately 5–7% Al^{3+} in the octahedral B-site (Hsu et al., 2012; Lin et al., 2013). Recent studies have shown that the B-site Fe^{3+} undergoes a spin transition at approximately 15–50 GPa (Catalli et al., 2010; Hsu et al., 2011; Lin et al., 2012; Mao et al., 2015; Liu et al., 2018) while the A-site iron ions experience local site distortions at ~ 45 GPa associated with an increase in the quadrupole splitting (Mao et al., 2017; Hsu and Wentzcovitch, 2014). The site distortion of A-site iron can affect the local electronic bonding characters resulting in distinct equation of state parameters and thermal conductivity of Bm (Mao et al., 2017; Hsieh et al., 2017). Spin transitions in Fp and Bm can also significantly change the partitioning of iron and magnesium between these minerals (Lin et al., 2013; Irifune et al., 2010; Xu et al., 2017). The partitioning coefficient $K_d = (\text{Fe}/\text{Mg})_{\text{Bm}}/(\text{Fe}/\text{Mg})_{\text{Fp}}$ in a pyrolitic mantle composition is ~ 0.8 at 30 GPa and drops to ~ 0.4 at 136 GPa corresponding to the core-mantle boundary (CMB) conditions (Irifune et al., 2010). This means that at the CMB, the proportion of iron atoms in Fp and Bm is about 3:2 and ferropericlase becomes the major iron carrier in the deeper lower mantle. Of particular interest to geochemistry are the potential effects of the spin transition and local site distortions on the vibrational properties and mean force constant $\langle F \rangle$ of the iron bonds. Indeed, equilibrium iron isotopic fractionation between phases is directly related to the difference in stiffness of iron bonds of coexisting minerals.

To explore the possible fractionation induced by the spin transition and lattice distortion under compression and quantify the magnitude of iron isotopic fractionation in the lower mantle, we measured the mean force constant $\langle F \rangle$ of the iron bonds in Fp and Bm samples with compositions relevant to the lower mantle. For this purpose, we pressurized the samples using diamond anvil cells (DACs) and measured their lattice vibrations using nuclear resonant inelastic X-ray scattering (NRIXS) spectroscopy. Synchrotron Mössbauer spectra were also collected to characterize the spin and valence states of iron in the samples.

2. Methods

2.1. Sample synthesis

Polycrystalline ^{57}Fe -enriched ferropericlase $((\text{Mg}_{0.75}\text{Fe}_{0.25})\text{O})$ was synthesized using the inter-diffusion of a mixture of MgO and metallic ^{57}Fe powder ($>98\%$ enrichment; Cambridge Isotopes) at approximately 1450 K for 8 h under a controlled CO_2 – CO atmosphere near the Fe–FeO redox buffer (Lin et al., 2006a). (Fe,Al)-bearing Bm single crystals $(\text{Mg}_{0.89}\text{Fe}_{0.024}^{2+}\text{Fe}_{0.096}^{3+}\text{Al}_{0.11}\text{Si}_{0.89}\text{O}_3)$ ($\text{Fe}^{3+}/\text{Fe}_{\text{tot}} = 0.8$) were synthesized from a mixture of MgSiO_3 , $\text{Mg}(\text{OH})_2$, Al_2O_3 , and ^{57}FeO powder ($>98\%$ enrichment; Cambridge Isotopes) in a Kawai-type apparatus at 24 GPa and 2023 K for 7 h at the Institute for Planetary Materials, Okayama University at Misasa, Japan (Okuchi et al., 2015; Mao et al., 2017). Poly-crystalline Bm $(\text{Mg}_{0.92}\text{Fe}_{0.07}^{2+}\text{Fe}_{0.02}^{3+}\text{Si}_{0.99}\text{O}_3)$ ($\text{Fe}^{3+}/\text{Fe}_{\text{tot}} = 0.25$ – 0.30) was synthesized from ^{57}Fe -enriched enstatite powder $(\text{Mg}_{0.9}\text{Fe}_{0.1}\text{SiO}_3)$ in a multi-anvil press at 24 GPa and 1673 K for an hour at the Geodynamic Research Center (GRC), Ehime University (Lin et al., 2006a). Another poly-crystalline Bm $(\text{Mg}_{0.74}\text{Fe}_{0.12}^{2+}\text{Fe}_{0.12}^{3+}\text{Si}_{0.98}\text{O}_3)$ ($\text{Fe}^{3+}/\text{Fe}_{\text{tot}} = 0.50$) was synthesized from laser heating ^{57}Fe -enriched enstatite powder $(\text{Mg}_{0.75}\text{Fe}_{0.25}\text{SiO}_3)$ sandwiched between NaCl pellets in a panoramic DAC. The sample was pressurized and heated at approximately 35 GPa and 1500 K for about 2 h at the GSECARS of the Advanced Photon Source, Argonne National Laboratory (Mao et al., 2011b). The chemical compositions, lattice parameters, and iron valence states of these samples were previously characterized using an electron micro-probe, X-ray diffraction, and Mössbauer spectroscopy (Mao et al., 2011b, 2017; Lin et al., 2012). Additional XRD measurements of the samples were performed at beamline 13-IDD of GSECARS to confirm their crystal structures at high pressures.

2.2. DAC preparation and synchrotron NRIXS measurements

We conducted *in situ* high pressure NRIXS experiments on ^{57}Fe -enriched ferropericlase $((\text{Mg}_{0.75}\text{Fe}_{0.25})\text{O})$ and bridgmanite $(\text{Mg}_{0.89}\text{Fe}_{0.024}^{2+}\text{Fe}_{0.096}^{3+}\text{Al}_{0.11}\text{Si}_{0.89}\text{O}_3, \text{Mg}_{0.92}\text{Fe}_{0.07}^{2+}\text{Fe}_{0.02}^{3+}\text{Si}_{0.99}\text{O}_3, \text{Mg}_{0.74}\text{Fe}_{0.12}^{2+}\text{Fe}_{0.12}^{3+}\text{Si}_{0.98}\text{O}_3)$ in diamond anvil cells (DACs) up to 104 GPa at sector 3ID-B of the Advanced Photon Source, Argonne National Laboratory. Each starting sample of about 10–20 μm in thickness and 20–30 μm in diameter was separately loaded into a sample chamber. The chamber was a hole drilled in a Be gasket embedded with a cubic BN gasket insert and squeezed between a pair of diamond anvils. We used panoramic diamond anvil cells as compression devices and the anvil culet size ranged from 400 μm flat to 150–300 μm beveled. For most of the experiments, we used a mini anvil (culet size 150 μm) or a partially perforated anvil (culet size 400 μm) facing the incident X-ray beam to reduce the intensity loss of the X-ray when it penetrated through the anvil; this also allowed us to collect the energy spectra with enhanced signal-to-noise ratio within a reasonable data collection time. Fp powder was loaded into a DAC using mineral oil as the pressure medium and a ruby sphere as the pressure calibrant. For Bm, two sets of NRIXS experiments were performed:

(1) A single-crystal (Fe,Al)-bearing Bm sample was polished to approximately 10–15 μm thick and then loaded into a DAC using mineral oil as the pressure medium and a ruby sphere as the pressure calibrant. The sample was measured at room temperature without laser annealing.

(2) The poly-crystalline Fe-bearing Bm samples were also polished and compressed between two NaCl pellets and laser-annealed to ~ 2000 K to release potential stress at each given pressure before the spectra were collected. The pressure was calibrated using ruby fluorescence spectra below 80 GPa. Above 80 GPa, XRD

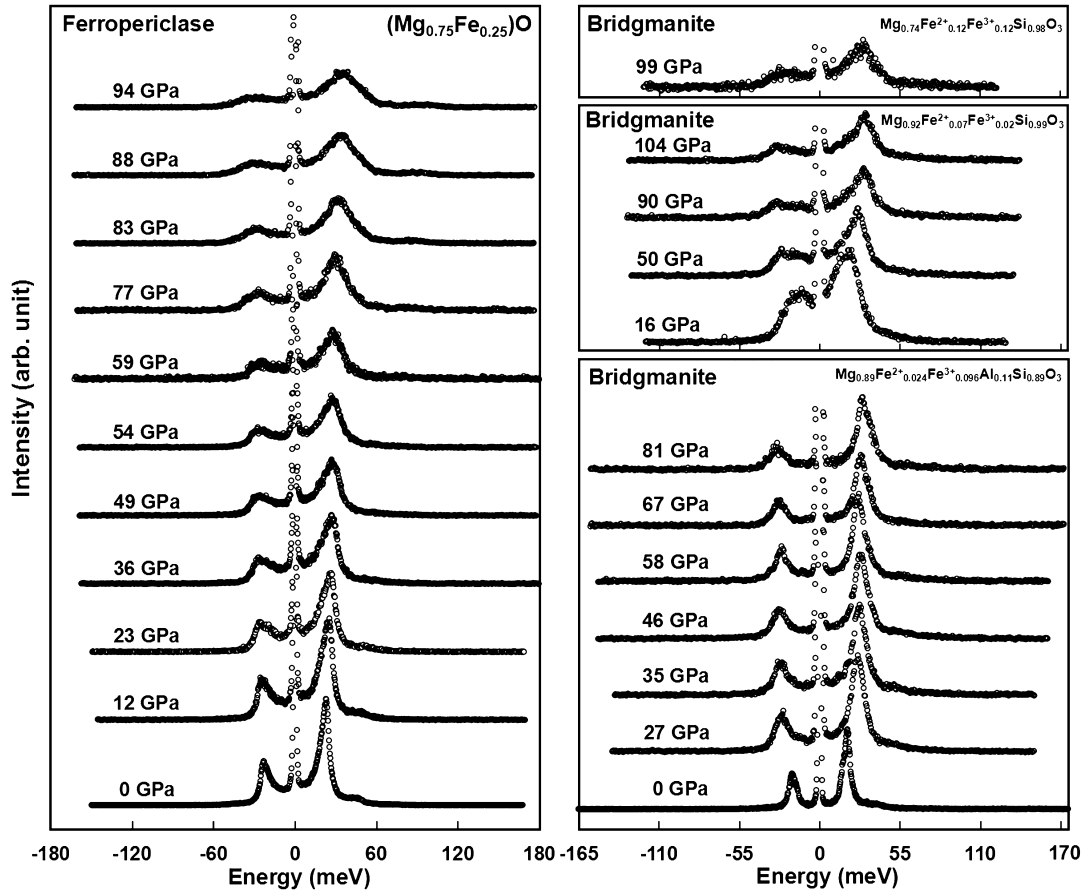


Fig. 1. NRIXS spectra of ferropericlase and bridgmanite at high pressures. The central peaks located near 0 meV correspond to the nuclear elastic scattering of the incident X-rays, while the other spectral features correspond to inelastically-scattered phonons either due to phonon creation ($E > 0$) or phonon annihilation ($E < 0$).

patterns of NaCl were collected and used as the pressure gauge, while the diamond Raman spectra were used as a secondary reference.

NRIXS spectra were scanned around the nuclear transition energy of ^{57}Fe (14.4125 keV) with a step size of 0.25–0.33 meV for the 1 meV energy resolution of the incident X-ray or 0.5–0.6 meV for the 2 meV energy resolution. The acquisition time was 3–5 s per energy step. The energy spectra of Fp below 70 GPa and (Fe,Al)-bearing Bm at ambient conditions were measured using the 1 meV energy resolution of the incident X-ray source, whereas the 2 meV energy resolution X-ray was used for the Fp sample above 70 GPa and all the Bm samples at high pressure. The incident X-ray source with a 2 meV resolution has a photon flux of 1×10^{10} photons/s, double of that of the X-ray source with a 1 meV resolution. The 2 meV monochromator was used for the high-pressure Bm measurements as (i) the samples had a relatively dilute Fe content and (ii) the high pressure increases the Lamb–Mössbauer factor, which means a decrease in the inelastic scattering probability, making the data collection even more challenging. Each NRIXS scan took about 1 to 1.5 h to complete, and 17–44 NRIXS scans (about 1–2 days of beamtime) were collected and combined in order to achieve good statistics for the inelastic signals. The energy spectra were collected over a broad energy scan range (for example from -160 to $+180$ meV for ferropericlase), which is crucial to capture the multi-phonon contributions and possible high-energy vibration modes that can influence the calculated $\langle F \rangle$ values.

2.3. Quality assessment and reliability of the force constant derivation

High-quality NRIXS data (Figs. 1, 2) with high signal/noise ratios were collected with sufficient numbers of energy scans (17–44)

over an extended range (± 120 to 200 meV). It is necessary to scan over wider energies at high pressure as the phonon modes shift to higher energies (Fig. 3).

Equilibrium iron isotopic fractionation is governed by the bonding strengths of the iron-bearing phases. The strength of the iron bonds is quantified using the mean force constant $\langle F \rangle$, which can be derived under the harmonic approximation from the analysis of the moments of the NRIXS energy spectra $S(E)$ using SciPhon (Dauphas et al., 2012, 2014, 2018; Blanchard et al., 2015). This method gives a better assessment of the experimental uncertainties and systematic errors than using the moments of the phonon density of states (Dauphas et al., 2012). In the quasi-harmonic lattice model, the mean force constant of iron $\langle F \rangle$ (in N/m) is related to the third moment of the NRIXS spectrum $S(E)$ through:

$$\langle F \rangle = \frac{M}{E_R \hbar} \int_{-\infty}^{+\infty} (E - E_R)^3 S(E) dE, \quad (1)$$

where M is the mass of the nuclear resonant isotope (^{57}Fe in this study), E is the energy difference between incident X-ray and the nuclear resonant energy E_0 (in meV), and $E_R = E_0^2/2Mc^2$ is the nuclear recoil energy (that is, 1.956 meV for ^{57}Fe , where $E_0 = 14.4125$ keV is the nuclear resonant energy of ^{57}Fe , and c is the speed of light). Within the harmonic approximation (interatomic potentials are quadratically related to atomic displacements), the $\langle F \rangle$ value of iron is independent of temperature. The β -factors can be calculated from $\langle F \rangle$ using the following relationship (Dauphas et al., 2012):

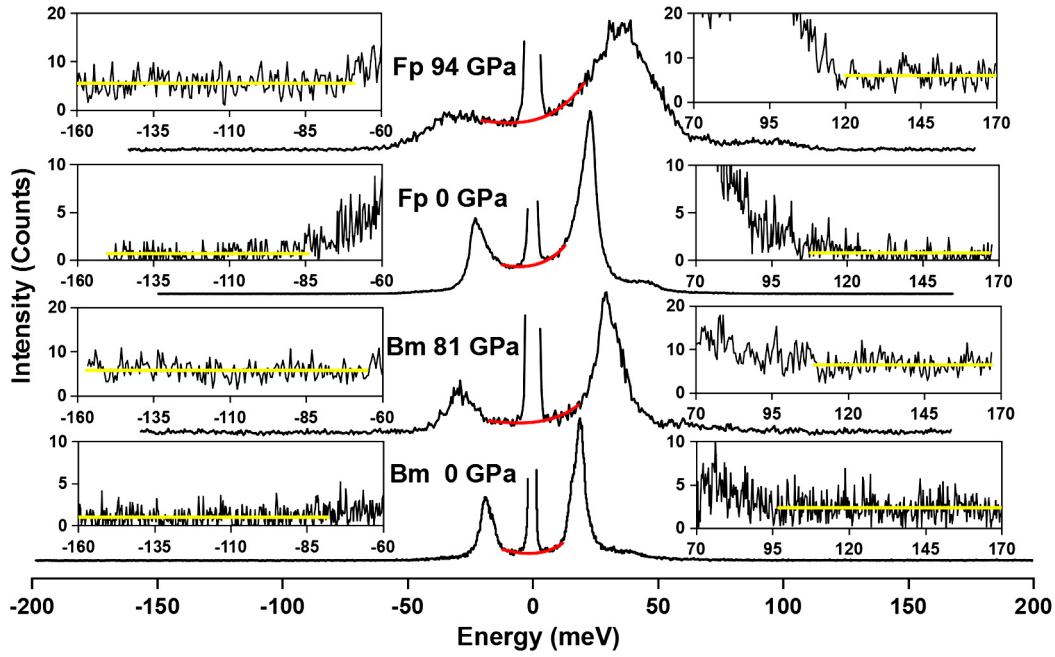


Fig. 2. Representative energy spectra of (Fe,Al)-bearing bridgmanite ($\text{Mg}_{0.89}\text{Fe}_{0.024}^{2+}\text{Fe}_{0.096}^{3+}\text{Al}_{0.11}\text{Si}_{0.89}\text{O}_3$) and ferropericlasite ($(\text{Mg}_{0.75}\text{Fe}_{0.25})\text{O}$) at high pressure. The central peaks located near 0 meV (partially truncated in the plots) correspond to the nuclear elastic scattering of the incident X-rays, while the other spectral features correspond to inelastically-scattered photons either due to phonon creation ($E > 0$) or phonon annihilation ($E < 0$). The red curves are interpolations of the energy spectra used to remove the elastic peak. The yellow horizontal lines are averages in the close-up views of the spectrum tails at low and high energy ends of the scans, which were interpolated for the subtraction of the baseline. Elastic peak removal and baseline subtraction were conducted using SciPhon (Dauphas et al., 2018). The extended energy range reaching ± 200 meV, together with the extremely low baseline level, were critical for an accurate evaluation of the force constants of iron in the samples at high pressure (see Fig. 3 for details). (For interpretation of the colors in the figure(s), the reader is referred to the web version of this article.)

$$1000 \ln \beta^{56\text{Fe}/54\text{Fe}} = 1000 \left(\frac{1}{M_{54\text{Fe}}} - \frac{1}{M_{56\text{Fe}}} \right) \frac{\hbar}{8k^2 T^2} \langle F \rangle$$

$$= 2904 \frac{\langle F \rangle}{T^2}, \quad (2)$$

where k is the Boltzmann's constant, \hbar is the reduced Planck constant, M represents the mass of an ^{54}Fe or ^{56}Fe nucleus and T is the absolute temperature in K. The β -factor, also known as the reduced partition function ratio, represents the ratio of ($^{56}\text{Fe}/^{54}\text{Fe}$) in the investigated iron-bearing phase, to the ($^{56}\text{Fe}/^{54}\text{Fe}$) in the ideal dissociated iron gas at equilibrium. Accordingly, by subtracting the $\ln \beta$ of phase A from that of phase B , we obtained the predicted equilibrium fractionation between two coexisting phases A and B (Urey, 1947),

$$\Delta^{56}\text{Fe}_{B-A}^{\text{eq}} = (\delta^{56}\text{Fe}_B - \delta^{56}\text{Fe}_A)_{\text{eq}}$$

$$= 1000 \ln \beta_B^{56\text{Fe}/54\text{Fe}} - 1000 \ln \beta_A^{56\text{Fe}/54\text{Fe}}$$

$$= 2904 \frac{\langle F \rangle_B - \langle F \rangle_A}{T^2}, \quad (3)$$

where $\delta^{56}\text{Fe}_A$ and $\delta^{56}\text{Fe}_B$ are the iron isotopic compositions of phases A and B , respectively, and $\Delta^{56}\text{Fe}_{B-A}^{\text{eq}}$ is the permil difference in the isotopic ratio ($^{56}\text{Fe}/^{54}\text{Fe}$) between phases A and B at thermodynamic equilibrium. The uncertainties of the derived mean force constant $\langle F \rangle$ in this study using SciPhon (Dauphas et al., 2018) include both statistical and systematic errors and are typically about 10–15% (Table 1).

3. Results

The iron force constant of Fp increases with pressure up to 60 GPa at a rate of $3.0 \text{ N m}^{-1} \text{ GPa}^{-1}$. Starting at 60 GPa, the force constant increases more rapidly at a rate of $8.6 \text{ N m}^{-1} \text{ GPa}^{-1}$ (Figs. 4 and 5). The spin transition of Fe^{2+} in Fp ($(\text{Mg}_{0.75}\text{Fe}_{0.25})\text{O}$)

Table 1

Mean force constant (F) of iron bonds in ferropericlasite and bridgmanite at high pressures (uncertainties include both statistical and systematic errors).

Composition	P (GPa)	Force constant (N m^{-1})
Ferropericlasite Fp25	0.0001	191.0 (± 8.0)
Ferropericlasite Fp25	12	219.0 (± 12.9)
Ferropericlasite Fp25	23	262.3 (± 15.8)
Ferropericlasite Fp25	36	278.5 (± 15.9)
Ferropericlasite Fp25	49	339.2 (± 20.7)
Ferropericlasite Fp25	54	333.1 (± 17.6)
Ferropericlasite Fp25	59	361.8 (± 41.6)
Ferropericlasite Fp25	77	475.1 (± 52.9)
Ferropericlasite Fp25	83	532.6 (± 28.4)
Ferropericlasite Fp25	88	586.6 (± 30.0)
Ferropericlasite Fp25	94	626.0 (± 31.4)
Bridgmanite Al-Bm11	0.0001	193.2 (± 18.9)
Bridgmanite Al-Bm11	27	297.8 (± 22.3)
Bridgmanite Al-Bm11	35	353.4 (± 36.3)
Bridgmanite Al-Bm11	46	448.6 (± 46.0)
Bridgmanite Al-Bm11	58	382.4 (± 42.6)
Bridgmanite Al-Bm11	67	330.2 (± 38.6)
Bridgmanite Al-Bm11	81	375.9 (± 42.1)
Bridgmanite Bm9	16	224.7 (± 20.0)
Bridgmanite Bm9	50	322.7 (± 28.0)
Bridgmanite Bm9	90	336.4 (± 32.7)
Bridgmanite Bm9	104	351.5 (± 32.1)
Bridgmanite Bm24	99	318.1 (± 50.0)

For composition abbreviations, Fp25 = $(\text{Mg}_{0.75}\text{Fe}_{0.25})\text{O}$, Al-Bm11 = $\text{Mg}_{0.89}\text{Fe}_{0.024}^{2+}\text{Fe}_{0.096}^{3+}\text{Al}_{0.11}\text{Si}_{0.89}\text{O}_3$, Bm9 = $\text{Mg}_{0.92}\text{Fe}_{0.07}^{2+}\text{Fe}_{0.02}^{3+}\text{Si}_{0.99}\text{O}_3$ and Bm24 = $\text{Mg}_{0.74}\text{Fe}_{0.12}^{2+}\text{Fe}_{0.12}^{3+}\text{Si}_{0.98}\text{O}_3$.

takes place around 60 GPa (Lin et al., 2005, 2013), as confirmed by synchrotron Mössbauer spectroscopy (SMS), which showed a transition from several quantum beats to a natural decay line implying the disappearance of quadrupole splitting in iron (Fig. 6). Across the spin transition, the unit cell volume collapses by $\sim 2\%$ and the Fe–O bond length decreases by at least 0.7% (Lin et al., 2013), respectively. The spin transition is visible in our experiments as a

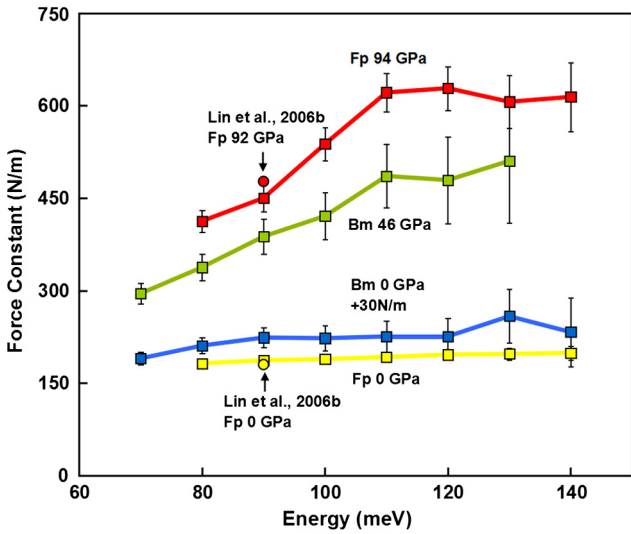


Fig. 3. Derived force constants $\langle F \rangle$ of iron bonds in ferropericlasite (Fp) and bridgmanite (Bm) at representative pressures. The results were calculated using various maximum energy ranges of the energy spectra from ± 60 meV to ± 140 meV. At ambient conditions, the derived $\langle F \rangle$ of both ferropericlasite and bridgmanite converge to a constant value at approximately 80 meV. The derived value converges at approximately 110 meV for the representative high pressure results of Fp at 94 GPa and Bm at 46 GPa, respectively. These analyses demonstrate the necessity for deriving reliable force constant values using a broader energy scan range in the high-pressure NRIXS energy spectra because phonon energies are expected to be elevated due to applied pressures. Results from Lin et al. (2006b) with ± 90 meV energy scan range are shown for comparison; the derived $\langle F \rangle$ of Fp using the energy spectra with a maximum energy range of ± 90 meV at 92 GPa is 477 N/m, which is significantly smaller than the value of 621 N/m derived in this study using an extended energy range of ± 110 meV.

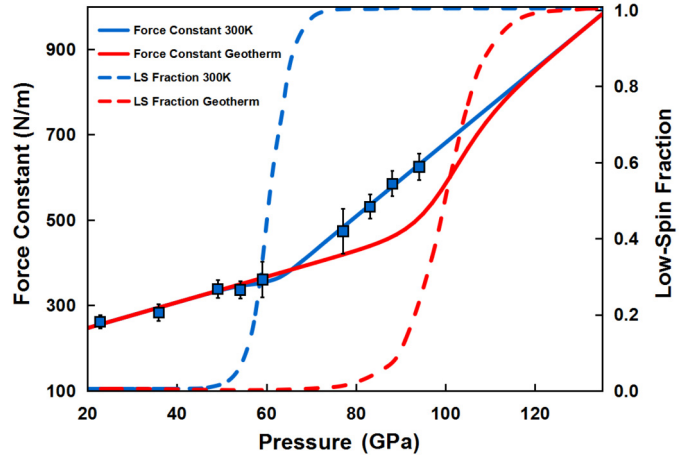


Fig. 5. Model of the iron force constant of iron bonds in ferropericlasite along an expected geotherm. Blue squares represent experimental results measured at 300 K in this study. The blue dashed line represents the low-spin iron fraction (Mao et al., 2011a) at 300 K whereas the red dashed line represents the low-spin iron fraction along a representative geotherm (Brown and Shankland, 1981). The low-spin fractions were used to fit the experimental data at 300 K (blue solid line) and to model the force constant of the iron bonds along an expected geotherm (Brown and Shankland, 1981) (red solid line).

change of the dependence of the $\langle F \rangle$ value with pressure. The $\langle F \rangle$ value of Bm increases with increasing pressure up to about 45 GPa at a rate of $\sim 5.5 \text{ N m}^{-1} \text{ GPa}^{-1}$. It slightly drops down to $\sim 350 \text{ N/m}$ and remains almost unchanged up to 100 GPa (Figs. 4 and S1). The $\langle F \rangle$ values of all Bm samples fall on the same trend, regardless of their $\text{Fe}^{3+}/\text{Fe}_{\text{tot}}$ ratios that range between 0.25 and 0.8 (Fig. 4). Finally we also included here the iron force constants $\langle F \rangle$ of silicate a basaltic glass previously determined to a maximum pressure of 64 GPa (Liu et al., 2017). Since there is no observable spin transition of iron in silicate glasses (Mao et al., 2014; Gu et al., 2012), we modeled the pressure dependence of $\langle F \rangle$ with a linear trend and extrapolated it to around 100 GPa. At pressures above 60 GPa, the LS Fp has a much larger $\langle F \rangle$ value than the Bm, basaltic glass (Liu et al., 2017) and iron alloys (Liu et al., 2017; Shahar et al., 2016) (Fig. 4), implying that heavy iron isotopes would be concentrated in LS Fp beneath the middle part of the lower mantle (Fig. 5).

4. Discussion

4.1. Determining the evolution of $\langle F \rangle$ in Bm and Fp as a function of P and T

The effect of the spin transition on $\langle F \rangle$ and the fractionation of isotopes in Fp has been demonstrated at 300 K. To address the fractionation of iron isotopes in the lower mantle, the measured mean force constant of the iron bonds $\langle F \rangle$ in Fp at high pressure and 300 K can be used to derive the pressure and temperature dependence of the force constant based on our prior knowledge on how iron partitions between low and high spins. We shall assume that the low-spin and high-spin iron atoms can be treated as independent components so that the mean force constant of iron can be calculated from the weighted average of the force constants of iron in the different spin states,

$$\langle F \rangle = \langle F \rangle_{LS} \times n_{LS} + \langle F \rangle_{HS} \times (1 - n_{LS}), \quad (4)$$

where n_{LS} is the fraction of the low-spin iron, and $\langle F \rangle_{HS}$ and $\langle F \rangle_{LS}$ are the force constants of iron in the high-spin (HS) and low-spin (LS) states. The LS iron fractions for Fp at different pressures and

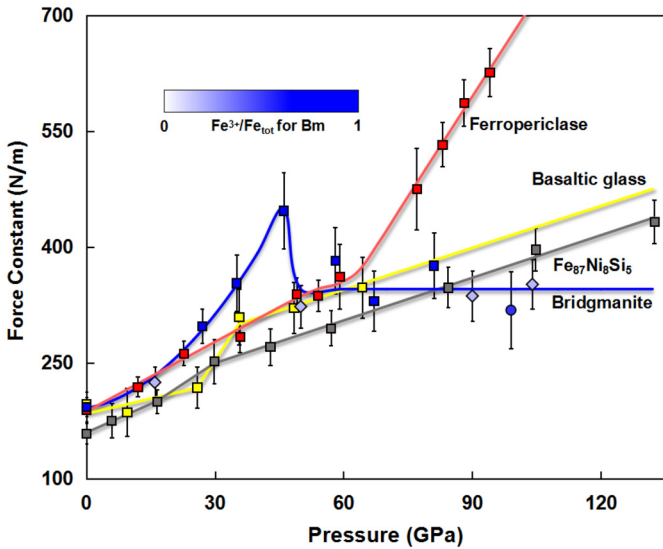


Fig. 4. Force constants $\langle F \rangle$ of iron bonds in ferropericlasite, bridgmanite, basaltic glass and $\text{Fe}_{87}\text{Ni}_8\text{Si}_5$ alloy as functions of pressure. Colored symbols represent experimentally derived force constants, while colored lines show simple fits to the experimental data to help guide the eyes. Ferropericlasite ($(\text{Mg}_{0.75}\text{Fe}_{0.25})\text{O}$) undergoes an iron spin transition at approximately 60 GPa, which significantly stiffens the force constant of the iron bonds (Fig. 5). The decrease in the force constant of iron in bridgmanite at approximately 45 GPa can be correlated with the iron local site change reported in previous studies (Hsu et al., 2010; Mao et al., 2017). Three different compositions of bridgmanite [$\text{Mg}_{0.89}\text{Fe}_{0.024}^{2+}\text{Fe}_{0.096}^{3+}\text{Al}_{0.11}\text{Si}_{0.89}\text{O}_3$ (blue squares), $\text{Mg}_{0.92}\text{Fe}_{0.07}^{2+}\text{Fe}_{0.02}^{3+}\text{Si}_{0.99}\text{O}_3$ (blue diamonds), $\text{Mg}_{0.74}\text{Fe}_{0.12}^{2+}\text{Fe}_{0.12}^{3+}\text{Si}_{0.98}\text{O}_3$ (blue circles)]; note that these are mostly A-site iron) were measured at high pressure. Data for the basaltic glass ($\text{Na}_{0.036}\text{Ca}_{0.220}\text{Mg}_{0.493}\text{Fe}_{0.115}\text{Al}_{0.307}\text{Ti}_{0.012}\text{K}_{0.002}\text{Si}_{0.834}\text{O}_3$) and $\text{Fe}_{87}\text{Ni}_8\text{Si}_5$ alloy are taken from Liu et al. (2017).

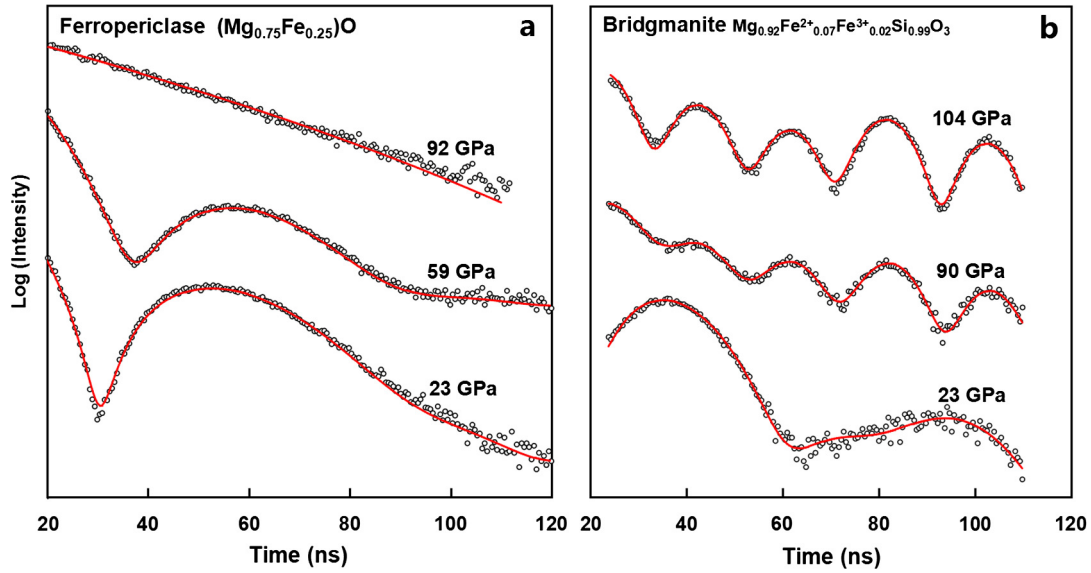


Fig. 6. Representative synchrotron Mössbauer spectra (SMS) of ferroprecipitate and bridgmanite at high pressures. The SMS data were fitted using the CONUSS software (Sturhahn, 2000). The quadrupole splitting (QS) of iron and its relative abundance obtained from fitting results can be used to reveal the pressure-induced evolution of spin states and local site environment of iron. **a** The low-spin iron in ferroprecipitate has a QS of 0 mm/s. Its abundance is 0% at 23 GPa, 48% at 59 GPa and 100% at 92 GPa, which demonstrates a gradual transition from the high-spin to the mixed-spin and eventually to the low-spin state. **b** Iron in bridgmanite with a very high QS up to 4 mm/s means strongly non-spherical distribution of electrons and is consistent with the distorted A-site (Hsu and Wentzcovitch, 2014; Lin et al., 2016; Mao et al., 2017). The bridgmanite at 23 GPa has 3 iron sites with QSs smaller than 2 mm/s. At 90 GPa, there are one site hosting 26% of iron with a QS of 4.1 mm/s and another site hosting 31% of iron with a QS of 2.7 mm/s. After further pressurized to 104 GPa, 53% population of iron has a QS of 4.1 mm/s and 32% of iron has a QS of 2.7 mm/s. This reveals a gradual transition from low-QS to high-QS in iron and an enhanced distortion of the A-site in bridgmanite at high pressure.

temperatures are reported in Mao et al. (2011a). The force constants of iron in different spin states can be expressed as a linear function of pressure:

$$\langle F \rangle_{LS} = a_{LS} \times P + b_{LS}, \quad \langle F \rangle_{HS} = a_{HS} \times P + b_{HS}, \quad (5)$$

where a and b are empirical fitting coefficients obtained by regressing the mean force constant $\langle F \rangle$ against P :

$$a_{HS} = 3.00 \pm 0.18 \text{ N m}^{-1} \text{ GPa}^{-1}, \quad b_{HS} = 186 \pm 6 \text{ N m}^{-1}, \\ a_{LS} = 8.62 \pm 0.61 \text{ N m}^{-1} \text{ GPa}^{-1}, \quad b_{LS} = -182 \pm 52 \text{ N m}^{-1}.$$

Note that LS iron is not stable below 60 GPa so it is inconsequential that b_{LS} is negative.

The force constant along an expected geotherm of the lower mantle (Brown and Shankland, 1981) was calculated using the pressure-temperature-dependent n_{LS} given in Mao et al. (2011a) and the results above (Fig. 5). With this new set of force constants, the β -factors of various phases along the expected geotherm (Brown and Shankland, 1981) were calculated from Eq. (2) and the isotopic fractionation between Fp and Bm is determined by Eq. (3). To estimate the isotopic composition of each phase, we also need to know how iron partitions between Fp and Bm, which allows us to write the following mass-balance relationship,

$$\delta^{56}\text{Fe}_{\text{mantle}} = \delta^{56}\text{Fe}_{\text{Fp}} \times n_{\text{Fp}} + \delta^{56}\text{Fe}_{\text{Bm}} \times n_{\text{Bm}}, \quad (6)$$

where n_{Fp} and n_{Bm} are the mass fraction of iron in ferroprecipitate and bridgmanite, respectively, $n_{\text{Fp}} + n_{\text{Bm}} = 1$. Combining equation (3) and (6), we calculated $\delta^{56}\text{Fe}_{\text{Fp}}$ and $\delta^{56}\text{Fe}_{\text{Bm}}$ (Fig. 7). In the calculation, we assumed that the lower mantle has a chondritic iron isotopic composition ($\delta^{56}\text{Fe}_{\text{mantle}} = 0\text{‰}$). The values of n_{Fp} and n_{Bm} are calculated from the previously determined iron partition coefficients by taking into account the effects of the spin transition in Fp and the Al-substitution in Bm for a pyrolitic mantle (Irifune et al., 2010). In a pyrolitic mantle, the presence of Al in the B-site of Bm tends to prevent ferric iron from partitioning into that

site so only the A-site iron needs to be considered. Furthermore, based on our data, the force constant of the iron cations in the A-site defines a single trend regardless of the proportions of ferric and ferrous iron. To the first order, our experimental determination of the $\langle F \rangle$ for the Bm is therefore appropriate to model iron isotopic fractionation in natural settings. Finally, there is a negligible amount of iron in CaSiO_3 silicate perovskite (Irifune, 1994) so we did not consider its partitioning into this phase.

Within this framework, our model indicates that little fractionation between Bm and Fp would be expected in the middle part of the lower mantle at depths between 1200 to 1800 km because of the counter effects between the iron local site change that induced softening in Bm and the pressure-enhanced $\langle F \rangle$ in Fp. The spin transition of iron in Fp starts at about 80 GPa along an expected geotherm (Brown and Shankland, 1981) such that Fp is expected to increasingly concentrate the heavy isotopes of iron compared with Bm at depths higher than 1800 km. Using the $\text{Fe}_{87}\text{Ni}_8\text{Si}_5$ alloy as an analogue for iron in the outer core (Liu et al., 2017), our modeling further shows that the equilibrium iron isotopic fractionation between Fp and metallic iron at CMB conditions (3570 K) (Nomura et al., 2014) is as large as 0.12‰, while the equilibrium isotopic fractionation between Bm and metallic iron is only -0.02‰ (Fig. 7). A similarly negligible fractionation is expected between a molten silicate and metallic iron (Liu et al., 2017). Taking into account the partitioning of iron between Fp and Bm under CMB conditions, we estimate an equilibrium core-mantle iron isotopic fractionation factor of $\sim 0.08\text{‰}$.

4.2. Bonding environment and force constant of iron in Bm at high pressure

The iron bonding environment and thus its force constants in Bm can be influenced by several factors including the site occupancy (A and B sites), spin and valence states, and lattice changes at high pressure. Our current understanding of the site occupancy in Bm is that the A-site hosts Fe^{2+} and Fe^{3+} while the B-site only accommodates Fe^{3+} (Catalli et al., 2010; Hsu et al., 2011;

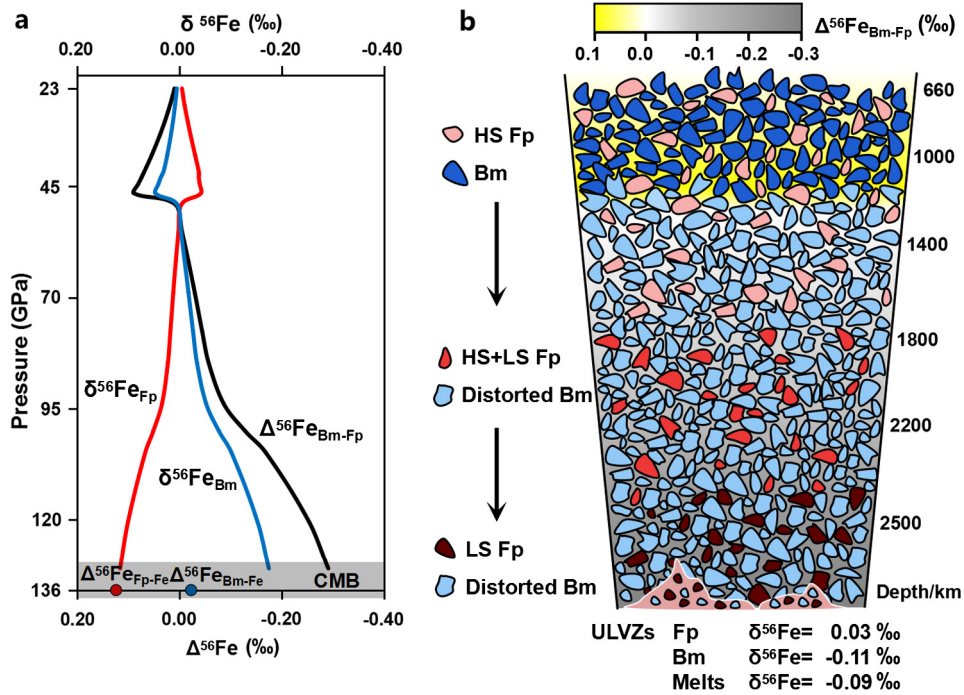


Fig. 7. Equilibrium $^{56}\text{Fe}/^{54}\text{Fe}$ isotope fractionation between ferropericlasite and bridgmanite along an expected lower-mantle geotherm. $\Delta^{56}\text{Fe}_{\text{Bm-Fp}} = \delta^{56}\text{Fe}_{\text{Bm}} - \delta^{56}\text{Fe}_{\text{Fp}} = 1000 \times (\ln \beta_{\text{Bm}}^{56/54}\text{Fe} - \ln \beta_{\text{Fp}}^{56/54}\text{Fe})$. The blue and red lines in a represent apparent ^{56}Fe isotopic profiles of bridgmanite and ferropericlasite across their respective spin and site distortion transitions (Fig. 6). The black line in a shows the equilibrium $^{56}\text{Fe}/^{54}\text{Fe}$ isotope fractionation between bridgmanite and ferropericlasite calculated along an expected geotherm (Brown and Shankland, 1981) by taking their partitioning coefficient in a pyrolytic composition into account (Irifune et al., 2010; Xu et al., 2017). The bulk mantle iron isotopic composition was assumed to be 0‰ relative to the international standard IRMM-014. The iron isotopic fractionation between the lower mantle and core phases is also indicated at the bottom of the plot. The CMB temperature was set at 3570 K (Nomura et al., 2014). **b** Schematics for iron isotopic difference of Fp and Bm in the bulk silicate Earth with a pyrolytic composition. Iron isotopic compositions of different phases in ULVZs were estimated at 3570 K (Nomura et al., 2014). The iron fraction ratio of phases in ULVZs was estimated to be 10:1:2 for Fp:Bm:melt considering melt fraction in the ULVZs and iron partitioning (Andraut et al., 2012; Xu et al., 2017; Hernlund and Jellinek, 2010).

Lin et al., 2013). The addition of Al^{3+} to Bm makes the B-site energetically unfavorable for Fe^{3+} such that (Fe,Al)-bearing Bm would contain A-site Fe^{3+} and B-site Al^{3+} via charge-coupled substitution (Hsu et al., 2012; Hummer and Fei, 2012). The current understanding of the spin states in Bm is that the B-site Fe^{3+} undergoes the HS–LS transition around 15–50 GPa (Catalli et al., 2010; Hsu et al., 2011; Mao et al., 2015; Liu et al., 2018) while Fe^{2+} and Fe^{3+} in A-site remain in the HS state throughout the lower mantle pressure range (Lin et al., 2016; Hsu et al., 2010, 2011). We should also note that an intermediate spin state of Fe^{2+} with very high QS at high pressure was also reported to occur (Lin et al., 2008) but not confirmed computationally (Hsu et al., 2010; Hsu and Wentzcovitch, 2014). Instead, what was found computationally (Hsu et al., 2010) was a change in iron *d*-orbital occupancy along with a lateral displacement of iron in the perovskite “A-site”. This change in Mössbauer quadrupole splitting (QS) corresponds to the theoretically identified displacement of iron in the A-site occurs between 30–60 GPa (Hsu et al., 2010). Beyond 60 GPa, the two states cannot be distinguished in the Mössbauer spectra, which suggested a double-well-like energetic structure for the low-QS and high-QS pair of states, with a final merging of both states into a single well at high pressures. Such a double-well structure was verified computationally (Hsu et al., 2010). State changes such as the low-QS to high-QS in a double-well type energetic structure should be very anharmonic.

To understand the effects of spin, valence, and lattice on the Fe–O force constants of our Bm samples at high pressure, we assume the charge-couple substitution mechanisms of $[\text{Fe}^{3+}]_A - [\text{Al}^{3+}]_B$ for the (Al,Fe)-bearing samples and $[\text{Fe}^{3+}]_A - [\text{Fe}^{3+}]_B$ for the Al-free samples. For example, based on the chemical formulae of our samples, their B site Fe^{3+} content should be $[\text{Mg}_{0.89}\text{Fe}_{0.024}^{2+}\text{Fe}_{0.096}^{3+}]_A[\text{Al}_{0.11}\text{Si}_{0.89}]_B\text{O}_3$, $[\text{Mg}_{0.92}\text{Fe}_{0.07}^{2+}\text{Fe}_{0.01}^{3+}]_A[\text{Fe}_{0.01}^{3+}$

$\text{Si}_{0.99}]_B\text{O}_3$ and $[\text{Mg}_{0.74}\text{Fe}_{0.12}^{2+}\text{Fe}_{0.10}^{3+}]_A[\text{Fe}_{0.02}^{3+}\text{Si}_{0.98}]_B\text{O}_3$. The latter might be an incomplete picture since charge balance in this Al-free sample implies in considerable amount of A-site vacancies. This reasonable assumption implies that there is very limited amount of B-site Fe^{3+} (up to few percent) in our (Al,Fe)-bearing and Al-free Bm samples. That is, the B-site spin transition in (Al,Fe)-bearing Bm would likely play a very minor role on the $\langle F \rangle$ results here. Therefore, the measured $\langle F \rangle$ values should predominantly represent a weight-averaged contribution from Fe^{2+} and Fe^{3+} bonding strengths in the A-site. We should note that Bm in the relevant lower-mantle composition is likely to contain significant amounts of Fe and Al such that the B-site Fe^{3+} should be very limited (Irifune et al., 2010; Hsu et al., 2012).

Both experimental and theoretical studies have documented significant change in the local iron environment in A-site Fe^{2+} at around 45 GPa associated with the low-QS to high-QS state change (Mao et al., 2017; Hsu et al., 2010; Boffa Ballaran et al., 2012) shown in the Mössbauer spectra in Fig. 6. The change in local environment and QS is also reflected in the lattice parameters indicating an increase in Si–O₆ octahedron tilting angle (Mao et al., 2017; Hirose et al., 2017). Our high-pressure Bm results show that the $\langle F \rangle$ value increases with increasing pressure up to approximately 40 GPa, which should be caused by the pressure-enhanced shortening of the interatomic distance of Fe^{2+} in the relatively low-QS state. At higher pressures, the lower value of $\langle F \rangle$ and the weak pressure dependence of the $\langle F \rangle$ value, an almost flat feature with increasing pressure, could be reflecting a balance between a negative effect on the $\langle F \rangle$ values from the enhanced site distortion and a positive effect from shortened inter-atomic distance. However, the “average” Fe^{2+} –O interatomic distance in the low-QS and high-QS states are quite similar (Fig. 2 in Hsu et al., 2010) with the low-QS site displaying a wider range of bond-lengths. Alterna-

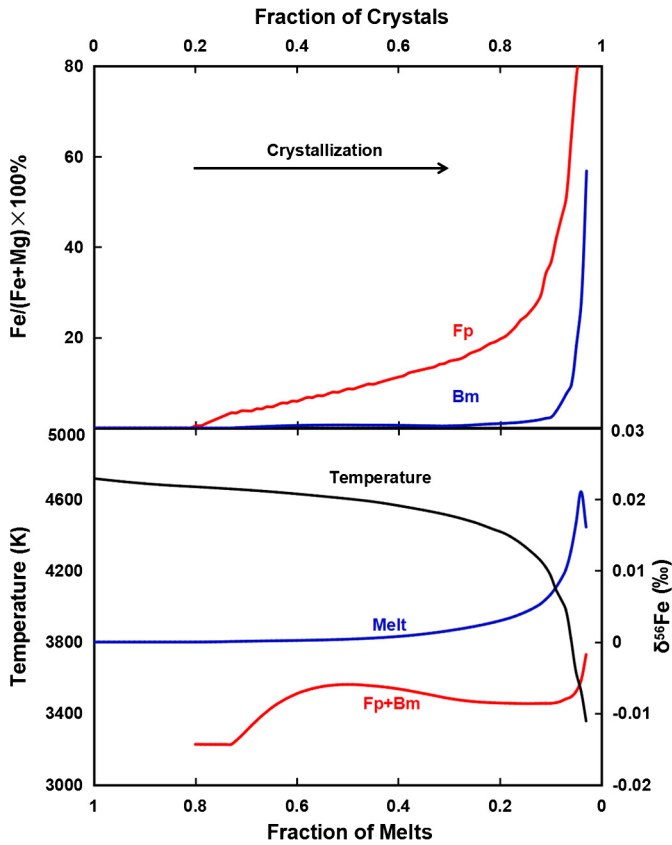


Fig. 8. Equilibrium $^{56}\text{Fe}/^{54}\text{Fe}$ isotope fractionation as a result of fractional crystallization in a deep magma ocean at 130 GPa. The magma ocean has an initial $\delta^{56}\text{Fe}$ value of 0‰ and the Fp and Bm crystals begin to solidify from the melt following a thermodynamic description of the crystallization sequence by Boukaré et al. (2015). The limited fractionation between the solids and melts is due to the extremely high temperature during the magma ocean stage.

tively, the dynamics of Fe^{2+} throughout the low-QS to the high-QS state change, a double-well like energetic structure changing into a single well at high pressures could be highly anharmonic. In this case, the harmonic expression for $\langle F \rangle$ and the harmonic calculation of phonon frequencies might not be appropriate. The dynamics of Fe^{2+} during the co-existence of these states during the co-existence of these states could be highly anharmonic and non-adiabatic. It is associated with a possibly small barrier between these states and different electronic occupancy of d orbitals in each side of the double well. At the moment, neither experimental nor theoretical methods are prepared to address this complex situation.

As shown in previous studies of silicate glasses (Dauphas et al., 2014) and spinels (Roskosz et al., 2015), the valence state of iron is also expected to influence the force constant of the host materials. These studies have found the iron force constant differences between ferrous and ferric end-members, $\Delta\langle F \rangle_{\text{Fe(III)}-\text{Fe(II)}}$, to be 152 ± 33 N/m, 145 ± 27 N/m and 104 ± 17 N/m, for basaltic glasses, rhyolitic glasses and spinels respectively. Our three Bm samples contained different $\text{Fe}^{3+}/\text{Fe}_{\text{tot}}$ ranging between 0.25 and 0.8, primarily in the A-site, and showed indistinguishable $\langle F \rangle$ results from each other.

Results of previous *ab initio* calculations can shed light on this indistinguishable force constants of Fe^{2+} and Fe^{3+} in the A-site. First, the average bond-lengths of Fe^{2+} in low QS and high QS states (Hsu et al., 2010), and Fe^{3+} in the HS state in the A-site (Hsu et al., 2011) are very similar. Only Fe^{3+} in the B-site, which is not abundant in our samples has a much shorter average bond-length. The similarity of average Fe–O bond-lengths of Fe^{3+} and Fe^{2+} in

the A-site can be reasoned on the basis of orbital occupancies. The bond-lengths depend strongly on the occupancy of e_g type orbitals which point toward the nearest neighbor oxygen atoms in an octahedral-like environment or nearly so. For both Fe^{2+} and Fe^{3+} in the HS state, as expected here, the d -electrons configurations are: $t_{2g}^4 e_g^2$ and $t_{2g}^3 e_g^2$, respectively, with the same occupancy of e_g states, therefore, resulting in similar Fe–O bond lengths. This symmetry classification of d -orbitals is not completely adequate because the symmetry is not octahedral but it is sufficient to say that the spin up electrons completely fill the spin up d -sub-shell with similar radii in both cases. The different ionization state of these ions plays a secondary role to electronic configuration (HS or LS) in determining the Fe–O bond-lengths. Not even the possible presence of “A-site” vacancies in one of our samples seems to affect this behavior.

4.3. Modeling the evolution of iron isotopic fractionation during magma ocean crystallization

The Earth is thought to have formed from collisions between large planetary embryos, which must have induced the formation of magma oceans (Ito et al., 2004; Walter et al., 2004). In particular, the Moon-forming giant impact may have induced widespread melting in the Earth. From a largely molten body to the present-day solid Earth, crystallization of the magma ocean would have shaped the Earth’s chemical structure and potentially fractionated iron isotopes in a manner analogous to what has been advocated for the Moon (Weyer et al., 2005; Poitrasson et al., 2004). Meanwhile, this large-scale melting event drastically redistributed iron within the different planetary reservoirs and it is possible that some Fe-rich regions became geodynamically isolated and eventually became a hidden iron isotope reservoir.

Here we use the fractionation factors of solid Fp and Bm together with a previously reported fractionation factor of a basaltic glass as an analogue to basaltic melts (Liu et al., 2017) to explore the possible consequences of a crystallization process happening in the deep lower mantle (Fig. 7). The $\langle F \rangle$ value for melts in the magma ocean is taken by extrapolating the $\langle F \rangle$ values of basaltic glass (Liu et al., 2017) to the relevant pressure assuming that the spin state of iron in silicate glass is unchanged at lower mantle conditions (Mao et al., 2014; Gu et al., 2012). The $\langle F \rangle$ value for the solid fraction was calculated as the weighted average of the force constants of Fp and Bm,

$$\langle F \rangle_{\text{sum}} = \langle F \rangle_{\text{Fp}} \cdot n_{\text{Fp}} + \langle F \rangle_{\text{Bm}} \cdot n_{\text{Bm}}, \quad (7)$$

where n_{Fp} and n_{Bm} are the proportions of iron in Fp and Bm in the solid fraction respectively, and $n_{\text{Fp}} + n_{\text{Bm}} = 1$.

We simulated the iron isotopic composition of melts and solid aggregates during the whole crystallization process (Fig. 8). Fractional crystallization and a mass-balance relationship were used in the model. The compositions of the solid and melt were calculated after each 1 wt% increment of crystallization. For the i th separation of crystals, the isotopic composition of crystals equilibrated with the remaining melts can be calculated by $\delta^{56}\text{Fe}_{\text{crystal-}i+1} = \delta^{56}\text{Fe}_{\text{melt-}i} + \Delta^{56}\text{Fe}_{\text{crystal-melt}}$, and based on the isotopic mass-balance we have:

$$\begin{aligned} \delta^{56}\text{Fe}_{\text{melt-}i+1} &= [\delta^{56}\text{Fe}_{\text{melt-}i} - (\delta^{56}\text{Fe}_{\text{melt-}i} + \Delta^{56}\text{Fe}_{\text{crystal-melt}}) \cdot n_{\text{crystal}}] / \\ &\quad (1 - n_{\text{crystal}}), \end{aligned} \quad (8)$$

$$\delta^{56}\text{Fe}_{\text{crystal-}i+1} = -\delta^{56}\text{Fe}_{\text{melt-}i+1} \cdot n_{\text{melt}} / (1 - n_{\text{melt}}), \quad (9)$$

where $\delta^{56}\text{Fe}_{\text{melt-}i}$ and $\delta^{56}\text{Fe}_{\text{melt-}i+1}$ are the iron isotopic composition of the melt before and after the i th increment of crystal

removal, $\Delta^{56}\text{Fe}_{\text{crystal-melt}}$ is the equilibrium iron isotopic fractionation between Fp and Bm aggregates and melts, n_{crystal} is the fraction of iron taken up by crystals at each step, $\delta^{56}\text{Fe}_{\text{crystals-}i+1}$ is the iron isotopic composition for accumulated Fp and Bm crystals after the i th increment and n_{melt} is the fraction of total iron in the remaining melt.

The compositional evolution of minerals crystallizing from the magma ocean was adapted from a previously reported thermodynamic model by Boukaré et al. (2015) (see Fig. 8). The crystallization starts from the liquidus phase Mg-Bm containing almost no iron. After about 20 wt% of the melt solidifying, Fe begins to be incorporated in the iron-bearing Fp. When ~ 27 wt% of the melt has crystallized, iron-bearing Bm appears. There is very limited iron isotopic fractionation in melts during most of the crystallization process because (i) iron is moderately incompatible and prefers to stay in the melt rather than in crystals (Andrault et al., 2012; Boukaré et al., 2015) and, (ii) the extreme high temperature suppresses the isotopic fractionation (Urey, 1947).

Over the whole crystallization process, melts are isotopically heavier than solids but the fractionation between solids and melts does not exceed +0.025‰. Much of that small fractionation would have presumably been erased by mantle mixing over Earth's history and would be hardly resolved given present analytical uncertainties. Our results thus suggest that crystallization of the magma ocean and associated equilibrium iron isotopic fractionation between melt and crystals is unlikely to have caused significant iron isotopic fractionation in any mantle reservoir.

5. Conclusion

We have measured the thermochemical and lattice dynamical properties of Fp and Bm at high pressure by applying the synchrotron technique of nuclear resonant inelastic X-ray scattering to samples loaded in diamond anvil cells. The results reveal a substantial change in the increase rate of the mean force constant of iron bonds at 60 GPa in Fp, corresponding to a spin transition of iron around that pressure. The mean force constant of Bm increases up to 45 GPa and then drops and remains constant above this pressure. This behavior is not easily understood but it could result from combined effects of strong anharmonicity in the dynamics of iron in the perovskite A-site and by a lattice distortion rather than a strengthening of the Fe–O bonds. The indistinguishable force constants of Fe^{2+} and Fe^{3+} in the A-site can be reasoned on the basis of the d -orbital occupancies and resulting comparable bond-lengths of these ions. The derived force constants are used to calculate the extent of the iron isotopic fractionation associated with magma ocean crystallization and the fractionation during this process was found to be minimal. Because of the significant differences in the iron force constants of the coexisting high pressure phases, strong iron isotopic heterogeneity is expected between coexisting minerals at high pressure but this heterogeneity may not be expressed in the isotopic geochemistry of the igneous rocks available at Earth's surface. Test of the iron isotope heterogeneity profile would be enabled by future isotopic analysis of Fp and Bm from the lower mantle.

Acknowledgements

We thank J. Yang, S. Fu, C. Zhang, N. Purevjav, T. Inoue, and S. Jacobsen for experimental assistance, T. Qin for helpful discussions, and F. O'toole for editing the manuscript. J.F. Lin acknowledges support from the U.S. National Science Foundation Geophysics and CSEDI Programs as well as the Center for High Pressure Science and Technology Advanced Research (HPSTAR). HPSTAR is supported by NSAF (Grant No. U1530402). N. Dauphas

acknowledges support from National Science Foundation (Cooperative Studies of the Earth's Deep Interior, EAR150259; Petrology and Geochemistry, EAR144495) and NASA (Laboratory Analysis of Returned Samples, NNX14AK09G; Cosmochemistry, OJ-30381-0036A and NNX15AJ25G). M. Roskosz acknowledges support from the French ANR (2011JS5600401, FRiHIDDA). W. Bi acknowledges the support from the Consortium for Materials Properties Research in Earth Sciences (COMPRES), the National Science Foundation (NSF) through Grant No. DMR-1104742. We acknowledge GSECARS and HPCAT of the APS for use of their diffraction and ruby facilities. This research used resources of the Advanced Photon Source, a U.S. Department of Energy (DOE) Office of Science User Facility operated for the DOE Office of Science by Argonne National Laboratory under Contract No. DE-AC02-06CH11357.

Appendix A. Supplementary material

Supplementary material related to this article can be found online at <https://doi.org/10.1016/j.epsl.2018.10.034>.

References

- Andrault, D., Petitgirard, S., Lo Nigro, G., Devidal, J.-L., Veronesi, G., Garbarino, G., Mezouar, M., 2012. Solid–liquid iron partitioning in Earth's deep mantle. *Nature* 487, 354–357. <https://doi.org/10.1038/nature11294>.
- Blanchard, M., Dauphas, N., Hu, M.Y., Roskosz, M., Alp, E.E., Golden, D.C., Sio, C.K., Tissot, F.L.H., Zhao, J., Gao, L., Morris, R.V., Fornace, M., Floris, A., Lazzeri, M., Balan, E., 2015. Reduced partition function ratios of iron and oxygen in goethite. *Geochim. Cosmochim. Acta* 151, 19–33.
- Boffa Ballaran, T.B., Kurnosov, A., Glazyrin, K., Frost, D.J., Merlini, M., Hanfland, M., Caracas, R., 2012. Effect of chemistry on the compressibility of silicate perovskite in the lower mantle. *Earth Planet. Sci. Lett.*, 181–190. <https://doi.org/10.1016/j.epsl.2012.03.029>.
- Boukaré, C.-E., Ricard, Y., Fiquet, G., 2015. Thermodynamics of the MgO–FeO–SiO₂ system up to 140 GPa: application to the crystallization of Earth's magma ocean. *J. Geophys. Res., Solid Earth* 120, 2015JB011929. <https://doi.org/10.1002/2015JB011929>.
- Bourdon, B., Roskosz, M., Hin, R.C., 2018. Isotope tracers of core formation. *Earth-Sci. Rev.* <https://doi.org/10.1016/j.earscirev.2018.04.006>.
- Brown, J.M., Shankland, T.J., 1981. Thermodynamic parameters in the Earth as determined from seismic profiles. *Geophys. J. Int.* 66, 579–596. <https://doi.org/10.1111/j.1365-246X.1981.tb04891.x>.
- Catali, K.C., Shim, S.H., Prakapenka, V.B., Zhao, J., Sturhahn, W., Chow, P., Xiao, Y., Liu, H., Cynn, H., Evans, W.J., 2010. Spin state of ferric iron in MgSiO₃ perovskite and its effect on elastic properties. *Earth Planet. Sci. Lett.* 289, 68–75. <https://doi.org/10.1016/j.epsl.2009.10.029>.
- Dauphas, N., Craddock, P.R., Asimow, P.D., Bennett, V.C., Nutman, A.P., Ohnenstetter, D., 2009. Iron isotopes may reveal the redox conditions of mantle melting from Archean to present. *Earth Planet. Sci. Lett.* 288, 255–267. <https://doi.org/10.1016/j.epsl.2009.09.029>.
- Dauphas, N., Hu, M.Y., Baker, E.M., Hu, J., Tissot, F.L., Alp, E.E., Roskosz, M., Zhao, J., Bi, W., Liu, J., 2018. SciPhon: a data analysis software for nuclear resonant inelastic X-ray scattering with applications to Fe, Kr, Sn, Eu and Dy. *J. Synchrotron Radiat.* 25. <https://doi.org/10.1107/S1600577518009487>.
- Dauphas, N., Roskosz, M., Alp, E.E., Golden, D.C., Sio, C.K., Tissot, F.L.H., Hu, M.Y., Zhao, J., Gao, L., Morris, R.V., 2012. A general moment NRIXS approach to the determination of equilibrium Fe isotopic fractionation factors: application to goethite and jarosite. *Geochim. Cosmochim. Acta* 94, 254–275. <https://doi.org/10.1016/j.gca.2012.06.013>.
- Dauphas, N., Roskosz, M., Alp, E.E., Neuville, D.R., Hu, M.Y., Sio, C.K., Tissot, F.L.H., Zhao, J., Tissandier, L., Médard, E., Cordier, C., 2014. Magma redox and structural controls on iron isotope variations in Earth's mantle and crust. *Earth Planet. Sci. Lett.* 398, 127–140. <https://doi.org/10.1016/j.epsl.2014.04.033>.
- Elardo, S.M., Shahar, A., 2017. Non-chondritic iron isotope ratios in planetary mantles as a result of core formation. *Nat. Geosci.* 10, 317–321. <https://doi.org/10.1038/ngeo2896>.
- Gu, C., Catali, K., Grocholski, B., Gao, L., Alp, E., Chow, P., Xiao, Y., Cynn, H., Evans, W.J., Shim, S.-H., 2012. Electronic structure of iron in magnesium silicate glasses at high pressure. *Geophys. Res. Lett.* 39, L24304. <https://doi.org/10.1029/2012GL053950>.
- Hernlund, J.W., Jellinek, A.M., 2010. Dynamics and structure of a stirred partially molten ultralow-velocity zone. *Earth Planet. Sci. Lett.* 296, 1–8. <https://doi.org/10.1016/j.epsl.2010.04.027>.
- Hirose, K., Sinmyo, R., Hernlund, J., 2017. Perovskite in Earth's deep interior. *Science* 358, 734–738. <https://doi.org/10.1126/science.aam8561>.

- Hsieh, W.-P., Deschamps, F., Okuchi, T., Lin, J.-F., 2017. Reduced lattice thermal conductivity of Fe-bearing bridgmanite in Earth's deep mantle. *J. Geophys. Res., Solid Earth* 122, 2017J014339. <https://doi.org/10.1002/2017J014339>.
- Hsu, H., Umamoto, K., Blaha, P., Wentzcovitch, R.M., 2010. Spin states and hyperfine interactions of iron in (Mg,Fe)SiO₃ perovskite under pressure. *Earth Planet. Sci. Lett.* 294, 19–26. <https://doi.org/10.1016/j.epsl.2010.02.031>.
- Hsu, H., Blaha, P., Cococcioni, M., Wentzcovitch, R.M., 2011. Spin-state crossover and hyperfine interactions of ferric iron in MgSiO₃ perovskite. *Phys. Rev. Lett.* 106, 118501. <https://doi.org/10.1103/PhysRevLett.106.118501>.
- Hsu, H., Yu, Y.G., Wentzcovitch, R.M., 2012. Spin crossover of iron in aluminous MgSiO₃ perovskite and post-perovskite. *Earth Planet. Sci. Lett.* 359–360, 34–39. <https://doi.org/10.1016/j.epsl.2012.09.029>.
- Hsu, H., Wentzcovitch, R.M., 2014. First-principles study of intermediate-spin ferrous iron in the Earth's lower mantle. *Phys. Rev. B* 90, 195205. <https://doi.org/10.1103/PhysRevB.90.195205>.
- Huang, F., Wu, Z., Huang, S., Wu, F., 2014. First-principles calculations of equilibrium silicon isotope fractionation among mantle minerals. *Geochim. Cosmochim. Acta* 140, 509–520. <https://doi.org/10.1016/j.gca.2014.05.035>.
- Hummer, D.R., Fei, Y., 2012. Synthesis and crystal chemistry of Fe³⁺-bearing (Mg,Fe³⁺) (Si, Fe³⁺)O₃ perovskite. *Am. Mineral.* 97, 1915–1921. <https://doi.org/10.2138/am.2012.4144>.
- Irifune, T., 1994. Absence of an aluminous phase in the upper part of the Earth's lower mantle. *Nature* 370, 131–133. <https://doi.org/10.1038/370131a0>.
- Irifune, T., Shinmei, T., McCammon, C.A., Miyajima, N., Rubie, D.C., Frost, D.J., 2010. Iron partitioning and density changes of pyrolite in Earth's lower mantle. *Science* 327, 193–195. <https://doi.org/10.1126/science.1181443>.
- Ito, E., Kubo, A., Katsura, T., Walter, M.J., 2004. Melting experiments of mantle materials under lower mantle conditions with implications for magma ocean differentiation. *Phys. Earth Planet. Inter.* 143–144, 397–406. <https://doi.org/10.1016/j.pepi.2003.09.016>.
- Lin, J.-F., Alp, E.E., Mao, Z., Inoue, T., McCammon, C., Xiao, Y., Chow, P., Zhao, J., 2012. Electronic spin states of ferric and ferrous iron in the lower-mantle silicate perovskite. *Am. Mineral.* 97, 592–597. <https://doi.org/10.2138/am.2012.4000>.
- Lin, J.-F., Gavriluk, A.G., Struzhkin, V.V., Jacobsen, S.D., Sturhahn, W., Hu, M.Y., Chow, P., Yoo, C.-S., 2006a. Pressure-induced electronic spin transition of iron in magnesiowüstite-(Mg,Fe)O. *Phys. Rev. B* 73, 113107. <https://doi.org/10.1103/PhysRevB.73.113107>.
- Lin, J.-F., Jacobsen, S.D., Sturhahn, W., Jackson, J.M., Zhao, J., Yoo, C.-S., 2006b. Sound velocities of ferropericlase in the Earth's lower mantle. *Geophys. Res. Lett.* 33, L22304. <https://doi.org/10.1029/2006GL028099>.
- Lin, J.-F., Speziale, S., Mao, Z., Marquardt, H., 2013. Effects of the electronic spin transitions of iron in lower mantle minerals: implications for deep mantle geophysics and geochemistry. *Rev. Geophys.* 51, 244–275. <https://doi.org/10.1002/rog.20010>.
- Lin, J.-F., Struzhkin, V.V., Jacobsen, S.D., Hu, M.Y., Chow, P., Kung, J., Liu, H., Mao, H., Hemley, R.J., 2005. Spin transition of iron in magnesiowüstite in the Earth's lower mantle. *Nature* 436, 377–380. <https://doi.org/10.1038/nature03825>.
- Lin, J.-F., Watson, H., Vankó, G., Alp, E.E., Prakapenka, V.B., Dera, P., Struzhkin, V.V., Kubo, A., Zhao, J., McCammon, C., Evans, W.J., 2008. Intermediate-spin ferrous iron in lowermost mantle post-perovskite and perovskite. *Nat. Geosci.* 1, 688–691. <https://doi.org/10.1038/ngeo0310>.
- Lin, J.-F., Mao, Z., Yang, J., Liu, J., Xiao, Y., Chow, P., Okuchi, T., 2016. High-spin Fe²⁺ and Fe³⁺ in single-crystal aluminous bridgmanite in the lower mantle. *Geophys. Res. Lett.* 43, 2016GL069836. <https://doi.org/10.1002/2016GL069836>.
- Liu, J., Dauphas, N., Roskosz, M., Hu, M.Y., Yang, H., Bi, W., Zhao, J., Alp, E.E., Hu, J.Y., Lin, J.-F., 2017. Iron isotopic fractionation between silicate mantle and metallic core at high pressure. *Nat. Commun.* 8, 14377. <https://doi.org/10.1038/ncomms14377>.
- Liu, J., Dorfman, S.M., Zhu, F., Li, J., Wang, Y., Zhang, D., Xiao, Y., Bi, W., Alp, E.E., 2018. Valence and spin states of iron are invisible in Earth's lower mantle. *Nat. Commun.* 9, 1284. <https://doi.org/10.1038/s41467-018-03671-5>.
- Mao, Z., Lin, J.-F., Liu, J., Prakapenka, V.B., 2011a. Thermal equation of state of lower-mantle ferropericlase across the spin crossover. *Geophys. Res. Lett.* 38, L23308. <https://doi.org/10.1029/2011GL049915>.
- Mao, Z., Lin, J.F., Scott, H.P., Watson, H.C., Prakapenka, V.B., Xiao, Y., Chow, P., McCammon, C., 2011b. Iron-rich perovskite in the Earth's lower mantle. *Earth Planet. Sci. Lett.* 309, 179–184. <https://doi.org/10.1016/j.epsl.2011.06.030>.
- Mao, Z., Lin, J.-F., Yang, J., Wu, J., Watson, H.C., Xiao, Y., Chow, P., Zhao, J., 2014. Spin and valence states of iron in Al-bearing silicate glass at high pressures studied by synchrotron Mössbauer and X-ray emission spectroscopy. *Am. Mineral.* 99, 415–423. <https://doi.org/10.2138/am.2014.4490>.
- Mao, Z., Wang, F., Lin, J.-F., Fu, S., Yang, J., Wu, X., Okuchi, T., Tomioka, N., Prakapenka, V.B., Xiao, Y., Chow, P., 2017. Equation of state and hyperfine parameters of high-spin bridgmanite in the Earth's lower mantle by synchrotron X-ray diffraction and Mössbauer spectroscopy. *Am. Mineral.* 102, 357–368. <https://doi.org/10.2138/am-2017-5770>.
- Mao, Z., Lin, J., Yang, J., Inoue, T., Prakapenka, V.B., 2015. Effects of the Fe³⁺ spin transition on the equation of state of bridgmanite. *Geophys. Res. Lett.* 42, 4335–4342. <https://doi.org/10.1002/2015GL064400>.
- Nomura, R., Hirose, K., Uesugi, K., Ohishi, Y., Tsuchiyama, A., Miyake, A., Ueno, Y., 2014. Low core–mantle boundary temperature inferred from the solidus of pyrolite. *Science*, 1248186. <https://doi.org/10.1126/science.1248186>.
- Okuchi, T., Purevjav, N., Tomioka, N., Lin, J.-F., Kuribayashi, T., Schoneveld, L., Hwang, H., Sakamoto, N., Kawasaki, N., Yurimoto, H., 2015. Synthesis of large and homogeneous single crystals of water-bearing minerals by slow cooling at deep-mantle pressures. *Am. Mineral.* 100, 1483–1492. <https://doi.org/10.2138/am-2015-5237>.
- Poitrasson, F., Halliday, A.N., Lee, D.-C., Levasseur, S., Teutsch, N., 2004. Iron isotope differences between Earth, Moon, Mars and Vesta as possible records of contrasted accretion mechanisms. *Earth Planet. Sci. Lett.* 223, 253–266. <https://doi.org/10.1016/j.epsl.2004.04.032>.
- Polyakov, V.B., 2009. Equilibrium iron isotope fractionation at core–mantle boundary conditions. *Science* 323, 912–914. <https://doi.org/10.1126/science.1166329>.
- Roskosz, M., Sio, C.K.L., Dauphas, N., Bi, W., Tissot, F.L.H., Hu, M.Y., Zhao, J., Alp, E.E., 2015. Spinel–olivine–pyroxene equilibrium iron isotopic fractionation and applications to natural peridotites. *Geochim. Cosmochim. Acta* 169, 184–199. <https://doi.org/10.1016/j.gca.2015.07.035>.
- Shahar, A., Schauble, E.A., Caracas, R., Gleason, A.E., Reagan, M.M., Xiao, Y., Shu, J., Mao, W., 2016. Pressure-dependent isotopic composition of iron alloys. *Science* 352, 580–582. <https://doi.org/10.1126/science.aad9945>.
- Sturhahn, W., 2000. CONUSS and PHOENIX: evaluation of nuclear resonant scattering data. *Hyperfine Interact.* 125, 149–172. <https://doi.org/10.1023/A:1012681503686>.
- Teng, F.-Z., Dauphas, N., Huang, S., Marty, B., 2013. Iron isotopic systematics of oceanic basalts. *Geochim. Cosmochim. Acta* 107, 12–26. <https://doi.org/10.1016/j.gca.2012.12.027>.
- Urey, H.C., 1947. The thermodynamic properties of isotopic substances. *J. Chem. Soc.*, 562–581. <https://doi.org/10.1039/JR9470000562>.
- Walter, M.J., Nakamura, E., Trønnes, R.G., Frost, D.J., 2004. Experimental constraints on crystallization differentiation in a deep magma ocean. *Geochim. Cosmochim. Acta* 68, 4267–4284. <https://doi.org/10.1016/j.gca.2004.03.014>.
- Wang, K., Moynier, F., Dauphas, N., Barrat, J.-A., Craddock, P., Sio, C.K., 2012. Iron isotope fractionation in planetary crusts. *Geochim. Cosmochim. Acta* 89, 31–45. <https://doi.org/10.1016/j.gca.2012.04.050>.
- Wentzcovitch, R.M., Justo, J.F., Wu, Z., Silva, C.R.S.D., Yuen, D.A., Kohlstedt, D.L., 2009. Anomalous compressibility of ferropericlase throughout the iron spin crossover. *Proc. Natl. Acad. Sci. USA* 106, 8447–8452. <https://doi.org/10.1073/pnas.0812150106>.
- Weyer, S., Anbar, A.D., Brey, G.P., Munker, C., Mezger, K., Woodland, A.B., 2005. Iron isotope fractionation during planetary differentiation. *Earth Planet. Sci. Lett.* 240, 251–264. <https://doi.org/10.1016/j.epsl.2005.09.023>.
- Wu, Z., Justo, J.F., Wentzcovitch, R.M., 2013. Elastic anomalies in a spin-crossover system: ferropericlase at lower mantle conditions. *Phys. Rev. Lett.* 110, 228501. <https://doi.org/10.1103/PhysRevLett.110.228501>.
- Xu, S., Lin, J.-F., Morgan, D., 2017. Iron partitioning between ferropericlase and bridgmanite in the Earth's lower mantle. *J. Geophys. Res.* 122, 2016J013543. <https://doi.org/10.1002/2016J013543>.